nature materials

SUPPLEMENTARY INFORMATION

DOI: 10.1038/NMAT3405

Quantum many-body interactions in digital oxide superlattices

Eric J. Monkman *,[1] Carolina Adamo *,[2] Julia A. Mundy,[3] Daniel E. Shai,[1] John W. Harter,[1] Dawei Shen,[1] Bulat Burganov,[1] David A. Muller,[3,4] Darrell G. Schlom,[2,4] and Kyle M. Shen[1,4,†]

[1]*Laboratory of Atomic and Solid State Physics, Department of Physics, Cornell University, Ithaca, New York 14853, USA*

[2]*Department of Materials Science and Engineering, Cornell University, Ithaca, New York 14853, USA*

[3]*School of Applied and Engineering Physics, Cornell University, Ithaca, New York 14853, USA*

[4]*Kavli Institute at Cornell for Nanoscale Science, Ithaca, New York 14853, USA*

Contents

Growth technique and structural characterization

Superlattices were grown using shuttered layer-by-layer deposition [1] on buffered-HF treated (100)-$SrTiO_3$ substrates [2] in a reactive molecular-beam epitaxy system equipped with reflection high-energy electron diffraction (RHEED) [3]. A substrate temperature of 750 °C and an oxidant (O_2+10% O_3) background partial pressure of 5×10^{-7} Torr, which was kept constant until the temperature of the substrate dropped below 250 °C, were used. All films measured in this study were 20 nm to 25 nm thick, and were terminated with n layers of $SrMnO_3$, where a layer corresponds to a formula-unit-thick layer along the growth direction. On reaching 250 °C, samples were immediately transferred in ultra-high vacuum ($\approx 10^{-10}$ Torr) to the ARPES cryostat and cooled. X-ray diffraction data for the $n = 1$ and $n = 3$ superlattices measured by ARPES are shown in Fig. S1.

In order to allow ARPES to probe the buried interface, our films were terminated with $(SrMnO_3)_n$ rather than the thicker $(LaMnO_3)_{2n}$ layer. To avoid surface effects arising from the polarity of the $LaMnO_3$ layers, our thin films were also made to be inversion symmetric by initiating growth on the $SrTiO_3$ substrates with $SrMnO_3$ layers. This introduces a very slight change of the global doping of the entire film by at most $\Delta x \leq 0.03$ away from $x = 1/3$.

The high structural quality of the film surface was verified after ARPES measurements with low energy electron diffraction (LEED). In Fig. S2a we present a LEED image taken from an $n = 3$ superlattice after remaining in the ARPES chamber for 8 days. We observe sharp diffraction peaks, a 2×4 surface reconstruction, and a 3×3 surface reconstruction also seen by RHEED during growth (Fig. S2c). This demonstrates the high crystallinity of the surface of our films, and proves that the pristine surface from growth is maintained throughout the transfer to our ARPES chamber and subsequent measurement. The origin of these surface reconstructions are not yet entirely understood, but we find that they are generic to the MnO_2 surface of the perovskite manganites, and not unique to our superlattices. Both the 2×4 and 3×3 reconstructions are observed on undoped $SrMnO_3$ films with MnO_2 surface termination (Fig. S2b). The 3×3 reconstruction is also routinely observed on the MnO_2 surface by reflection high-energy electron diffraction (RHEED) during MBE growth of both the superlattices and $La_{1-x}Sr_xMnO_3$ films (e.g. Fig. S2c). We also observe the 2×4 surface reconstruction on $La_{0.7}Sr_{0.3}MnO_3$ films, along with other groups

* These authors contributed equally to this work.

†Author to whom correspondence should be addressed: kmshen@cornell.edu

DOI: 10.1038/NMAT3XXX

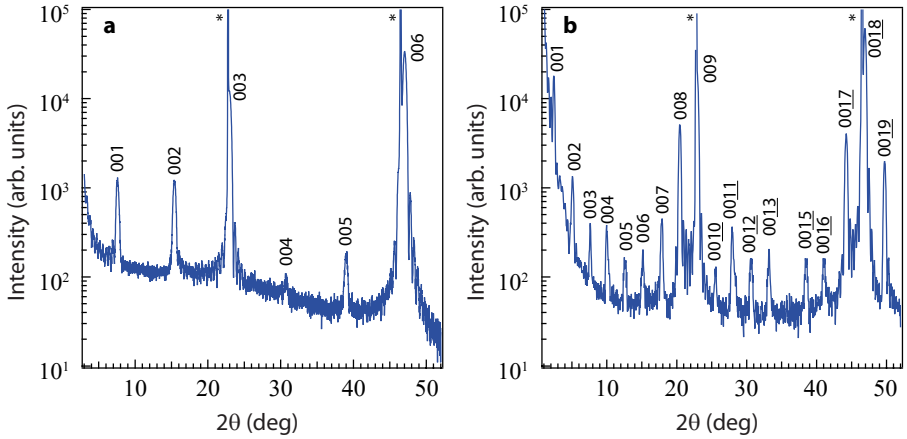

Figure S1: X-ray diffraction curves of the (**a**) $n = 1$ and (**b**) $n = 3$ superlattices measured by ARPES. Diffraction peak indices are indicated for the films; substrate peaks are denoted by the *.

who find the same reconstruction on $La_{0.6}Sr_{0.4}MnO_3$ films grown by pulsed-laser deposition [4]. As mentioned in the main text, we do not observe signatures of these reconstructions in our ARPES data, and since they are present for both insulating and metallic films of widely varying composition and structure, they cannot be responsible for the spectra that we report. On the other hand, we do observe a weak $c(2 \times 2)$ reconstruction in our Fermi surface maps. This reconstruction is expected to exist throughout the superlattice due to its stability in $LaMnO_3$ [5], and so we do not attribute it to being solely a surface effect.

Electron energy loss spectroscopic imaging (EELS-SI), recorded from cross sectional specimens in the 100 keV NION UltraSTEM, was used to investigate three of the films measured by ARPES. The Mn concentration is the integrated Mn-$L_{2,3}$ edge, the La concentration is the integrated La-$M_{4,5}$, and the Ti concentration is the integrated Ti-$L_{2,3}$. As shown in Fig. 1d-f, Fig. S3, Fig. S4, and Fig. S5 all samples show a clear repetition of the $LaMnO_3$ and $SrMnO_3$ layers corresponding to the $n = 1$, 2, and 3 layering patterns. The high angle annular dark field scanning transmission electron microscopy (HAADF-STEM) images show a coherent interface between the film and substrate, free of defects (Fig. S3). An apparent slight modulation of the interfaces observable in EELS images is an artifact of sample drift during acquisition, and is absent in the more quickly acquired HAADF-STEM images. May et al. [6] found a strong structural asymmetry between $LaMnO_3/SrMnO_3$ and $SrMnO_3/LaMnO_3$ interfaces in $(LaMnO_3)_{11.8}/(SrMnO_3)_{4.4}$ superlattices, which was found to significantly effect the superlattice's magnetic properties. We note that in our extensive EELS investigations, we observed no signatures of such an asymmetry for $n = 1$ and $n = 2$ superlattices (Fig. S4), and only a very weak asymmetry for $n = 3$ when examined over very wide regions (Fig. S5). Thus, we do not expect that the asymmetry reported in ref. [6] adversely effects the properties of the films reported in our study. Although we do not understand the difference between our samples and those of May et al., the asymmetric roughening trend would be consistent with a Stranski-Krastanov growth mode for the $LaMnO_3$ layer, with the onset for island formation somewhere between 6 (ours) and 11 layers (May's).

Tight-binding parametrization

The $(LaMnO_3)_{2n}/(SrMnO_3)_n$ superlattice contains $3n$ inequivalent Mn sites, and a full tight-binding parametrization would contain $6n$ e_g orbitals and many free parameters. In the interest of using the simplest possible model to represent our data, and noting that we only wish to parametrize the bandstructure at the interface, we expect a model containing one $d_{3z^2-r^2}$ and one $d_{x^2-y^2}$ state to be adequate. Thus, we use a model defined by [7];

$$t_{\pm a\hat{x}} = \frac{t_1}{4}\begin{pmatrix} 1 & -\sqrt{3} \\ -\sqrt{3} & 3 \end{pmatrix} \qquad t_{\pm a\hat{y}} = \frac{t_1}{4}\begin{pmatrix} 1 & \sqrt{3} \\ \sqrt{3} & 3 \end{pmatrix} \qquad t_{\pm a\hat{z}} = \alpha t_1 \begin{pmatrix} 1 & 0 \\ 0 & 0 \end{pmatrix}$$

$$t_{\pm a\hat{x}\pm a\hat{y}} = \frac{t_2}{2}\begin{pmatrix} 1 & 0 \\ 0 & -3 \end{pmatrix} \qquad t_{\pm a\hat{x}\pm a\hat{z}} = \frac{\alpha t_2}{2}\begin{pmatrix} -2 & \sqrt{3} \\ \sqrt{3} & 0 \end{pmatrix} \qquad t_{\pm a\hat{y}\pm a\hat{z}} = \frac{\alpha t_2}{2}\begin{pmatrix} -2 & -\sqrt{3} \\ -\sqrt{3} & 0 \end{pmatrix}$$

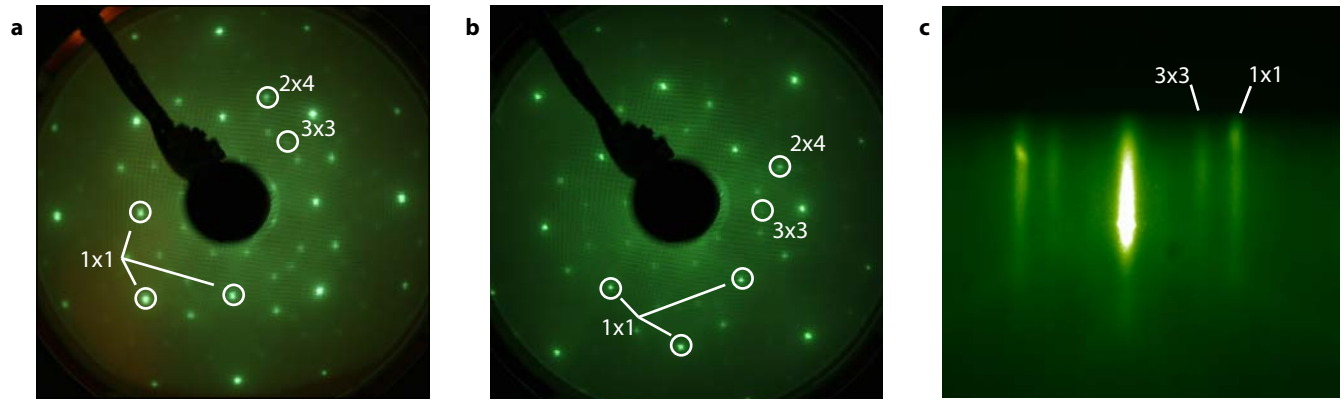

Figure S2: LEED pattern taken with 100 eV electrons from an $n = 3$ superlattice (**a**) and a $SrMnO_3$ film (**b**), both with MnO_2 surfaces. Diffraction peaks corresponding to the unreconstructed surface and two reconstructions are indicated. Note that the $SrMnO_3$ LEED pattern is rotated by 45 degrees. **c,** RHEED pattern from the MnO_2 surface of the same $n = 3$ film during growth.

Sample	t_1	t_2	μ	α
alloy	0.87	$0.13t_1$	$-1.13t_1$	1
$n = 1$	1.1	$0.15t_1$	$-1.33t_1$	0.45±0.25
$n = 2$	0.97	$0.10t_1$	$-1.31t_1$	0.22±0.09
$n = 3$	1.2	$0.08t_1$	$-1.38t_1$	≤0.16

Table I: The tight-binding parameters that best fit our experimental data. Error bars for α are estimated from the uncertainty in fits of the electron-pocket FS.

With $d_{3z^2-r^2} = [\,1\;\;0\,]$, $d_{x^2-y^2} = [\,0\;\;1\,]$, and with a chemical potential μ. We have elected to use a single parameter $0 \leq \alpha \leq 1$ to represent the suppression of hopping in the z direction caused by the superlattice, which is assumed to effect nearest neighbor and next-nearest neighbor hopping equally.

This model was fit to our ARPES data for each superlattice and for data from the random alloy $La_{1-x}Sr_xMnO_3$ (data not shown) using our determination of the Fermi surface to fit t_2, μ, and α. The procedure for fitting our data is as follows. First, we use the sharply-resolved hole pocket at E_F to determine t_2/t_1 and μ/t_1. This feature is dominated by segments of the hole pocket near $k_z = \pi/a$, which are essentially independent of α. With the values of t_2/t_1 and μ/t_1 now determined by the hole pocket data, we then determine α by fitting data from the electron pocket, which is very sensitive to the value of α. We find that this two-step approach produces much more reliable fit parameters than an unconstrained fit where both Fermi surface sheets are fit simultaneously by allowing t_2/t_1, μ/t_1, and α to vary freely. The determination of the size of the electron pocket is the dominant source of uncertainty in determining α and hence the orbital polarization, which is made more complicated by k_z-smearing that results in an electron pocket with a combination of sharp peaks and a broader background [8]. Therefore, we estimate the uncertainty in the size of the electron pocket by taking as an upper bound the FWHM of the intensity around Γ, and as a lower bound, the separation between two peak maxima around Γ, as shown in Fig. S6a. For the $n = 3$ superlattice, where no electron pocket Fermi surface is resolved, we provide only an upper bound for α that lifts the electron pocket completely above E_F. We then use the uncertainty in the size of our electron pockets to obtain uncertainty estimates for α shown in Table I, also represented in the error bars for the orbital polarization in Fig. 2d. The remaining parameter, t_1, is then fit to the dispersion of the hole pocket away from E_F. Note that the value of t_1 has no effect on the Fermi surfaces in Fig. 2a-c or the numerical values reported in Fig. 2d, since it only results in an overall scaling of the energy units. Our extracted tight-binding parameters for all four samples are displayed in Table I.

DOI: 10.1038/NMAT3XXX

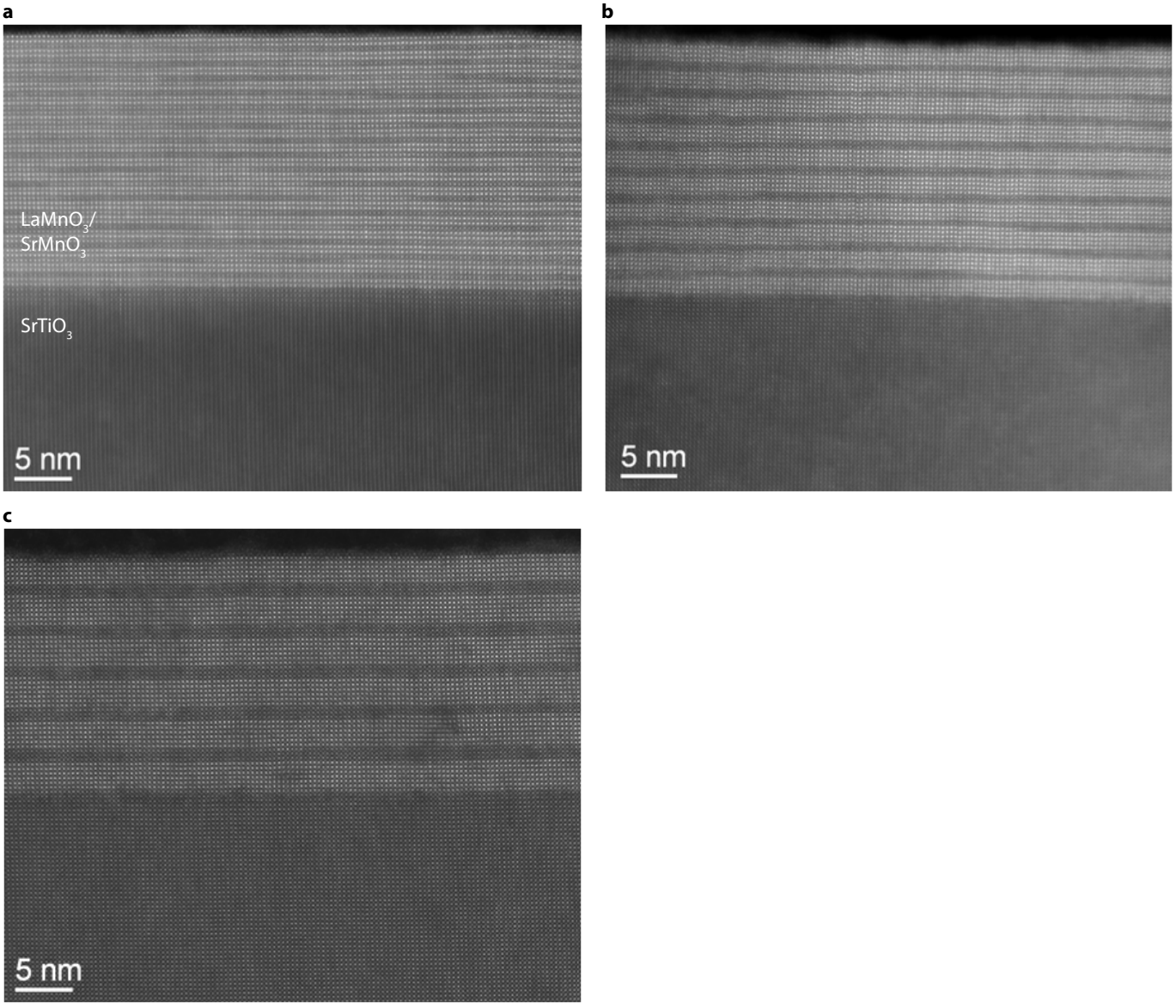

Figure S3: HAADF-STEM images of the same (**a**) $n = 1$, (**b**) $n = 2$, and (**c**) $n = 3$ $(LaMnO_3)_{2n}/(SrMnO_3)_n/SrTiO_3$ films measured by ARPES. The films show a coherent interface between the film and the substrate free of observable defects and a clear repetition of the $LaMnO_3$ and $SrMnO_3$ layering to form the desired superlattices.

ARPES on $LaMnO_3$ and $SrMnO_3$

To ensure that the results reported in the main text are not artifacts from the $LaMnO_3$ or $SrMnO_3$ surfaces, we have performed ARPES experiments on a series of control samples: a 10 unit cell thick $LaMnO_3$ film with MnO_2 surface termination, an 8 unit cell thick $SrMnO_3$ film with SrO termination, an 8 unit cell thick $SrMnO_3$ film with MnO_2 termination, and a 6 unit cell thick $SrMnO_3$ film with MnO_2 termination. To avoid charging effects due to the insulating nature of these films, all samples were grown on 0.5% Nb-doped $SrTiO_3$ substrates and measured at room temperature. Samples were chosen to be thin enough to avoid charging while being thick enough to minimize any signal from the $SrTiO_3$ interface.

In all cases, we observe dispersive valence band spectra and sharp LEED patterns, indicative of the high quality of the films. As expected, we did not observe any appreciable or dispersive spectral weight within 0.4 eV of E_F for any of the control samples, as shown in Fig. S7. Therefore, we can safely conclude that the dispersive states near E_F arise from the $LaMnO_3/SrMnO_3$ interface. The valence band of the MnO_2 terminated $SrMnO_3$ films qualitatively

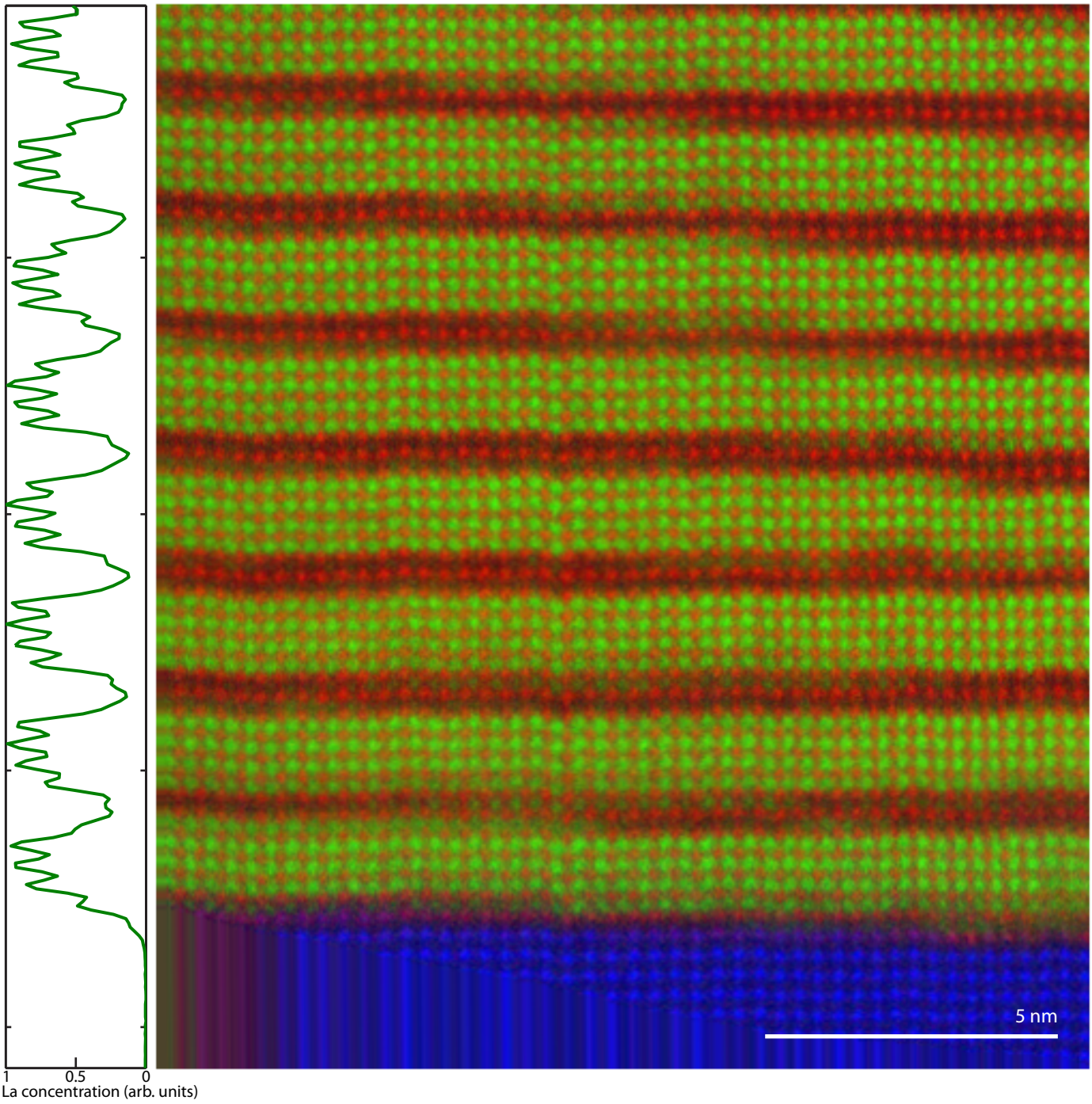

Figure S4: EELS map over a wide field of view from an $n = 2$ $(LaMnO_3)_{2n}/(SrMnO_3)_n/SrTiO_3$ film measured by ARPES, showing La in green, Mn in red, and Ti in blue. Steps in the $LaMnO_3/SrMnO_3$ interfaces follow the terraces of the $SrTiO_3$ substrate. Left: the La concentration along the growth direction of the film (obtained by integrating the La-$M_{4,5}$ intensity across the image) showing sharp interfaces between $LaMnO_3$ and $SrMnO_3$ lacking any systematic asymmetry. Streaks in the bottom left corner of the EELS map are an artifact of post-acquisition drift correction.

resemble those of the superlattices at higher binding energies, due to the $SrMnO_3$ termination of the superlattices. As expected, we also observe the tail of the $SrMnO_3$ valence band (occupied Mn t_{2g} and O $2p$ states) at approximately 0.3 eV binding energy in both the $SrMnO_3$ and superlattices (Figs. S7c and d). Nevertheless, only the superlattices exhibit the well-defined, near E_F bands which are the focus of our manuscript, confirming that these states arising intrinsically from the $LaMnO_3/SrMnO_3$ interface and cannot be a spurious effect.

DOI: 10.1038/NMAT3XXX

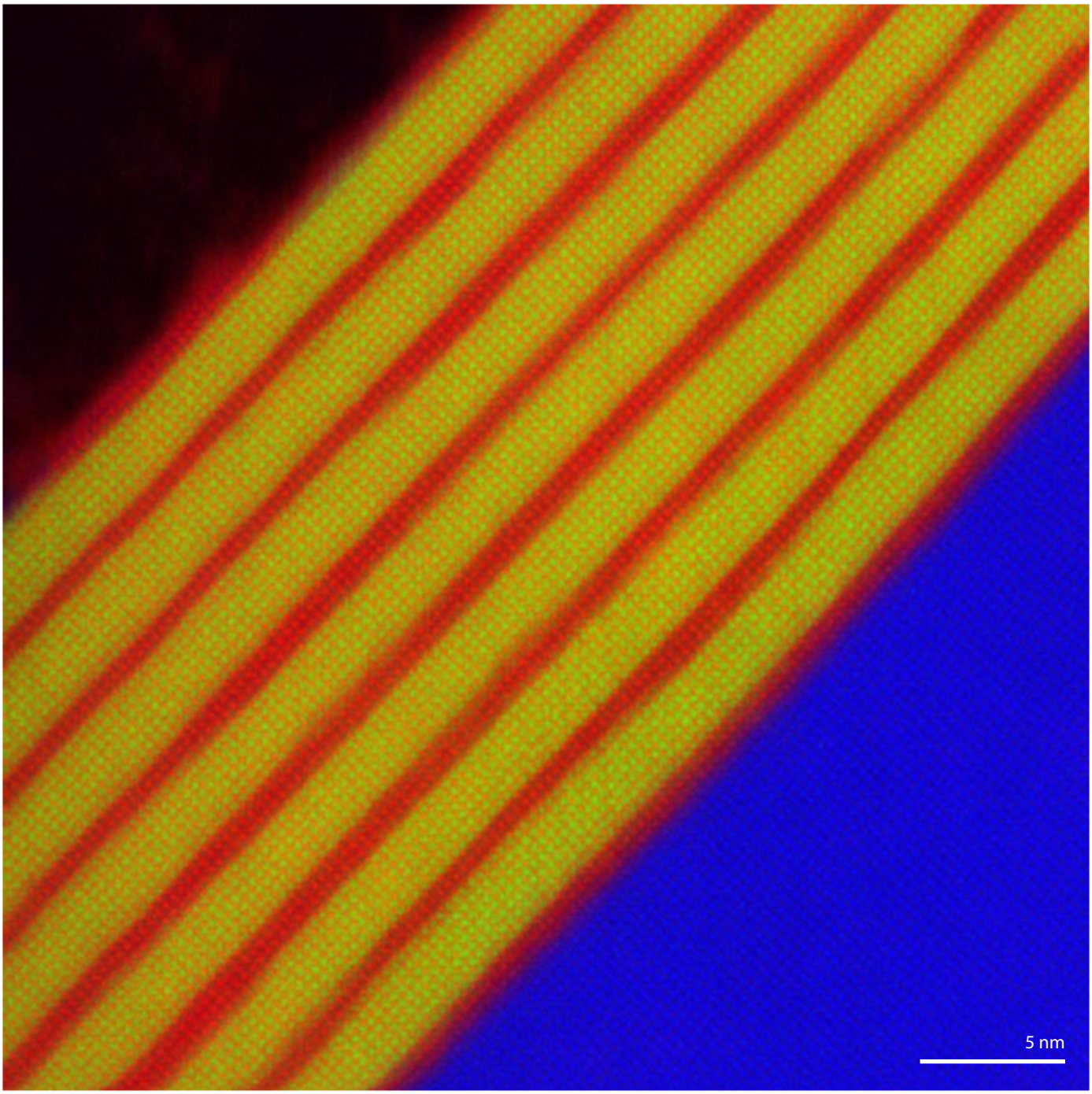

Figure S5: EELS map over a wide field of view from an $n = 3$ $(LaMnO_3)_{2n}/(SrMnO_3)_n/SrTiO_3$ film measured by ARPES, showing La in green, Mn in red, and Ti in blue. The irregularity of the topmost surface in this image is an artifact of the preparation procedure for EELS and HAADF-STEM measurements, and does not reflect the topmost surface of the as-grown film.

ARPES background subtraction and k_z-dispersion

The data presented in Fig. 3a-c and Fig. 4a of the main text have had a non-dispersive background subtracted to more clearly highlight the dispersive bands. In Fig. S8 we present the raw data used in these plots, as well as electron-pocket data for the $n = 1$ and 3 superlattices. Plots and analyses in Fig. 3d,e, Fig. 4b and all other figures use un-subtracted data. The intensity of the ARPES data in Figs. 3-5, and S8 were normalized at 12 eV binding

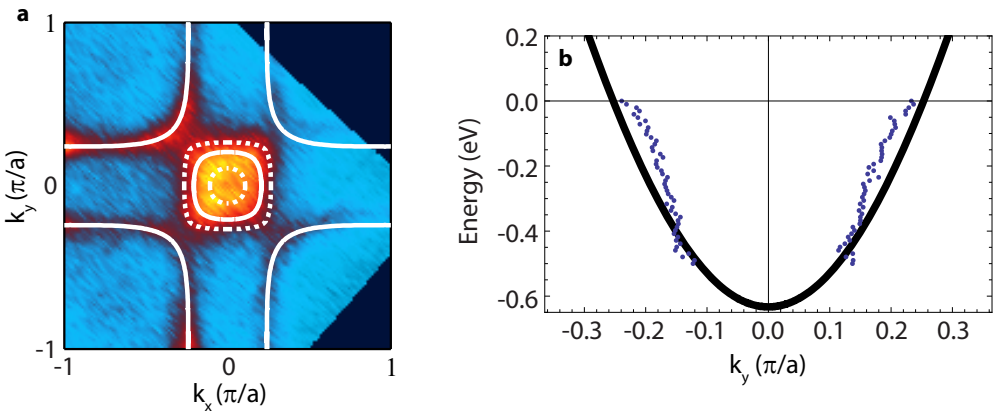

Figure S6: An example of the tight-binding fit to experimental data, this data taken from the $n = 2$ superlattice. **a,** The FS overlaid with the hole pocket and electron pocket fits, which are used to determine t_2, μ, α. The dotted-line shows the upper and lower bounds for the size of the electron pocket. **b,** The dispersion of the hole pocket at $k_x = 0.55\pi/a$, which is used to determine t_1. Black lines are the tight-binding fit.

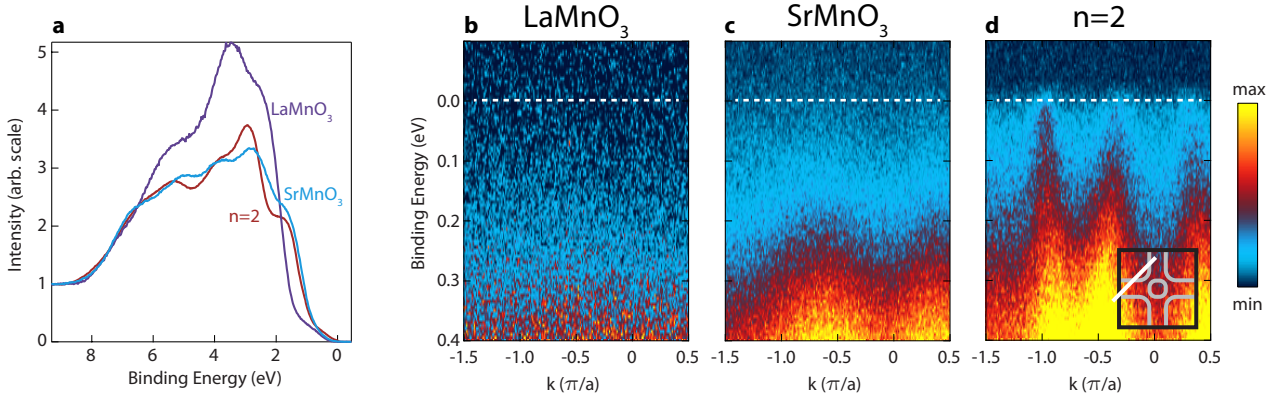

Figure S7: ARPES from $LaMnO_3$ and $SrMnO_3$. **a,** Valence bands of $LaMnO_3$ and $SrMnO_3$ films (10 and 8 u.c. thick respectively, MnO_2 terminated), compared with the $n = 2$ superlattice. **b,c,** ARPES data for the $LaMnO_3$ and $SrMnO_3$ films showing a lack of dispersive features within 0.4 eV of E_F. **d,** ARPES data for the $n = 2$ superlattice showing the dispersive e_g-derived bands discussed in the main text and responsible for this film's metallic behavior.

energy. In Fig. 1a-c, the average intensity for the three superlattices are set to be equal at 0.1 eV to facilitate the comparison of the momentum distributions.

The effect of a finite k_z-dispersion on ARPES spectra of the manganites is well documented for the 3D perovskite [8]. In that case, the electron pocket at the BZ center is largely smeared-out due to its significant dispersion along k_z, while the hole pocket around the BZ corner is expected to show more well defined features due to its largely non-k_z-dispersive walls. For the superlattices, with a BZ that is a factor of $3n$ smaller along k_z, the smearing in the k_z direction should extend across the BZ. Thus, in our analysis of the bandstructure we assume that the effects of k_z smearing dominate the photoemission, and that any sharply-defined features seen in ARPES correspond to the sections of bandstructure with the least k_z-dispersion.

[1] Haeni, J. H., Theis, C. D. & Schlom, D. G. RHEED Intensity Oscillations for the Stoichiometric Growth of $SrTiO_3$ Thin Films by Reactive Molecular Beam Epitaxy. *J. Electroceram.* **4,** 385-391 (2000).
[2] Koster, G., Kropman, B. L., Rijnders, G. J. H. M., Blank, D. H. A. & Rogalla, H. Quasi-ideal strontium titanate crystal surfaces through formation of strontium hydroxide. *Appl. Phys. Lett.* **73,** 2920-2922 (1998).
[3] Adamo, C. *et al.* Electrical and magnetic properties of $(SrMnO_3)_n/(LaMnO_3)_{2n}$ superlattices. *Appl. Phys. Lett.* **92,** 112508 (2008).

DOI: 10.1038/NMAT3XXX

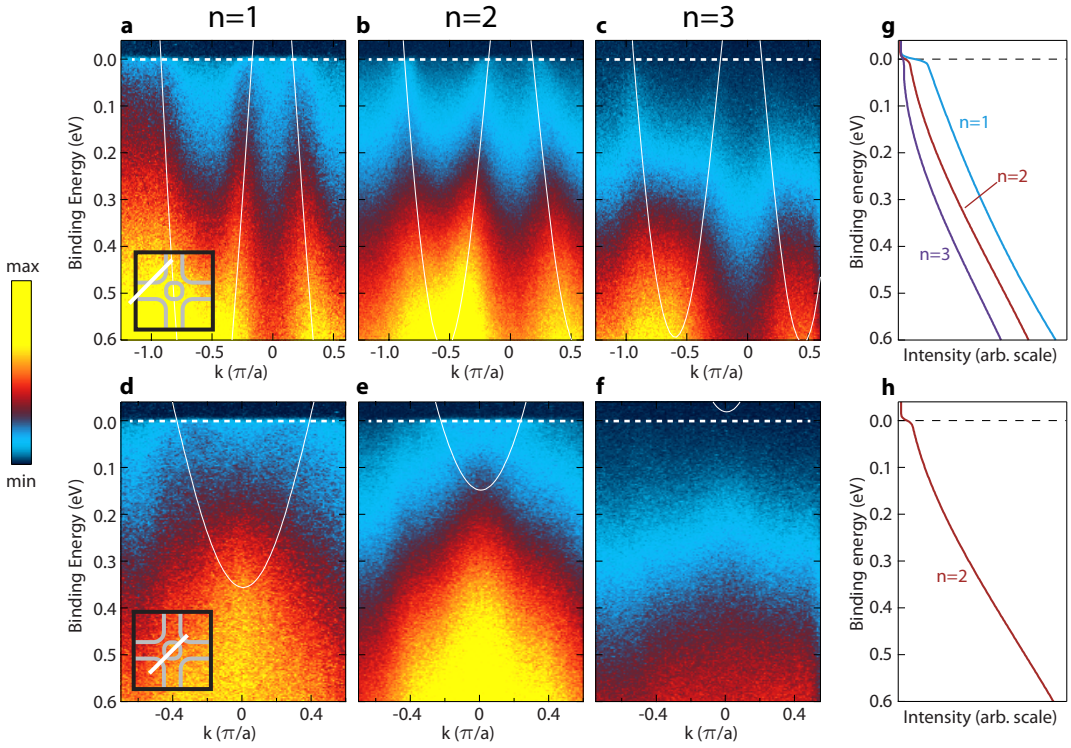

Figure S8: Raw ARPES data corresponding to the background-subtracted data shown in Figs. 3 and 4 of the main text. **a-c,** Hole pocket data corresponding to Fig. 3a-c, with TB bands overlaid as white lines. **d-f,** Electron pocket data for the $n = 1$, 2, and 3 superlattices respectively, with TB bands for only the electron pockets overlaid as white lines. Panel e corresponds to the data shown in Fig. 4a. **g,h,** The non-dispersive backgrounds subtracted from the ARPES data shown in the main text.

[4] Horiba, K. *et al.* A high-resolution synchrotron-radiation angle-resolved photoemission spectrometer with *in situ* oxide thin film growth capability. *Rev. Sci. Instrum.* **74,** 3406 (2003).

[5] Nanda, B. R. K. & Satpathy, S. Electronic and Magnetic Structure of the $(LaMnO_3)_{2n}/(SrMnO_3)_n$ Superlattices. *Phys. Rev. B* **79,** 054428 (2009).

[6] May, S. J. *et al.* Magnetically asymmetric interfaces in a $LaMnO_3/SrMnO_3$ superlattice due to structural asymmetries. *Phys. Rev. B* **77,** 174409 (2008).

[7] Ederer, C., Lin, C. & Millis, A. J. Structural distortions and model Hamiltonian parameters: From LSDA to a tight-binding description of $LaMnO_3$. *Phys. Rev. B* **76,** 155105 (2007).

[8] Krempasky, J. *et al.* Effects of three-dimensional band structure in angle- and spin-resolved photoemission from half-metallic $La_{2/3}Sr_{1/3}MnO_3$. *Phys. Rev. B* **77,** 165120 (2008).